Available online at www.sciencedirect.com
SCIENCE DIRECT®
Combustion and Flame 144 (2006) 494–512
Combustion and Flame
www.elsevier.com/locate/combustflame

Experimental investigation of stabilization mechanisms in turbulent, lifted jet diffusion flames

L.K. Su [a,*], O.S. Sun [a], M.G. Mungal [b]

[a] *Applied Fluid Imaging Laboratory, Department of Mechanical Engineering, Johns Hopkins University, Baltimore, MD 21218, USA*

[b] *Thermosciences Division, Mechanical Engineering Department, Stanford University, Stanford, CA 94305, USA*

Received 21 January 2005; received in revised form 18 August 2005; accepted 21 August 2005

Available online 10 October 2005

Abstract

Simultaneous planar-laser induced fluorescence (PLIF) and particle image velocimetry (PIV) provide a comprehensive view of the molecular mixing and velocity fields in the stabilization region of turbulent, lifted jet diffusion flames. The Mie scattering medium for PIV is a glycerol–water fog, which evaporates at elevated temperatures and allows inference of the location of the high-temperature interface at the flame base. The jet Reynolds numbers vary from 4400 to 10,700. The mixing and velocity fields upstream of the flame base evolve consistently with non-reacting jet scaling. Conditional statistics of the fuel mole fraction at the instantaneous high-temperature interface show that the flame stabilization point does not generally correspond to the most upstream point on the interface (called here the *leading point*), because the mixture there is typically too lean to support combustion. Instead, the flame stabilization point lies toward the jet centerline relative to the leading point. Conditional axial velocity statistics indicate that the mean axial velocity at the flame front is $\approx 1.8 S_L$, where S_L is the stoichiometric laminar flame speed. The data also permit determination of the scalar dissipation rates, χ, with the results indicating that χ values near the high-temperature interfaces do not typically exceed the quenching value. Thus, the flame stabilization process is more consistent with theories based on partial fuel–air premixing than with those dependent on diffusion flame quenching. We propose a description of flame stabilization that depends on the large-scale organization of the mixing field.

Keywords: Liftoff; Nonpremixed; Partially premixed; Turbulent jet flame; PLIF; PIV

1. Introduction

The turbulent, lifted jet diffusion flame is characteristic of many practical combustion systems, such as gas burners for power generation. Fig. 1 depicts the lifted, co-flowing jet diffusion flame system. Fuel issues from a nozzle, at velocity u_0, surrounded by an air co-flow with velocity u_∞. When u_0 is sufficiently high, the flame stands off from the nozzle exit, and the upstream part of the flame assumes a hollow shape. The base of a turbulent lifted flame experiences strong, random oscillations, which complicates analysis of the flow system. Among early efforts to describe the flame stabilization mechanism, the main point of contention was the degree of fuel–air premixing upstream of the flame base. One theory postulated

* Corresponding author.
E-mail address: lsu@jhu.edu (L.K. Su).

0010-2180/$ – see front matter
doi:10.1016/j.combustflame.2005.08.010

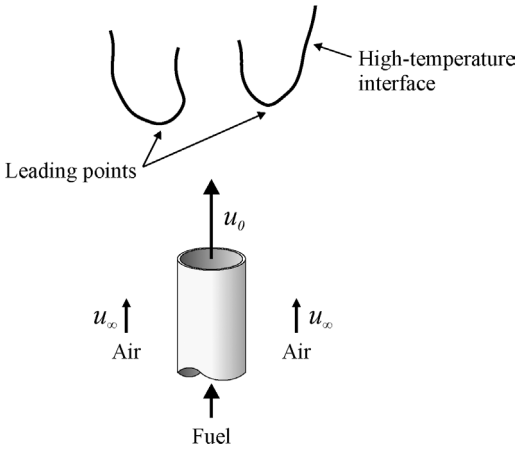

Fig. 1. A schematic of the lifted, co-flowing jet diffusion flame. The high-temperature interface (the figure depicts a two-dimensional section of the interface) is marked by large temperature gradients between the unburned gases and the hot combustion products. This interface may, but does not necessarily, mark the actual flame location. The leading points are defined as the most upstream positions on the high-temperature interface, on each side of the jet centerline.

that the upstream fuel–air mixture should be treated as premixed, and that the flame stabilized on the contour of mean stoichiometric mixture at the point where the local axial flow velocity matched the relevant turbulent flame speed [1]. An alternate theory held that combustion at the flame base took place in thin, laminar nonpremixed flamelets, and that the flame stabilized where the local strain rate along instantaneous stoichiometric surfaces fell below the flamelet extinction value [2].

As these theories have been assessed, it has become clear that the true stabilization picture involves a compromise between fully premixed and nonpremixed combustion. Prior progress in this area was thoroughly reviewed by Pitts [3]. Recent experimental work has benefited substantially from the advent of planar imaging methods that allow the flame location to be determined simultaneously with measurements of the velocity or scalar mixing fields. This allows the consideration of velocity and scalar values at the instantaneous flame base. (In earlier single-point measurements, velocity and scalar values were found at fixed locations, and thus could not be conditioned on the instantaneous flame location.) Schefer et al. [4], Kelman et al. [5], and Watson et al. [6], for example, made planar measurements of fuel concentrations upstream of the flame zone in methane–air lifted flames. Schefer et al. and Kelman et al. used combined Rayleigh and Raman scattering to measure the upstream methane concentrations, while Watson et al. used Rayleigh scattering only. To infer the instantaneous flame zone location, Schefer et al. and Watson et al. used simultaneous planar laser-induced fluorescence (PLIF) of the CH combustion radical; Kelman et al. used PLIF of the OH radical. All three studies show clearly that the fuel–air mixtures upstream of the flame are subject to significant turbulent fluctuations, and cannot be classified as fully premixed. Schefer et al. and Watson et al. further contend that scalar dissipation rates immediately upstream of the flame are insufficient to quench the combustion, casting doubt on the model of nonpremixed, flamelet combustion, though the adequacy of the spatial resolution of those measurements is not certain.

In light of these and similar results, the notion of partially premixed combustion has emerged. The canonical partially premixed flame system is the so-called triple flame [7,8]. Essential to the formation of a triple flame is a gradient in the cross-stream profile of the fuel mixture fraction, ranging from fuel-rich to fuel-lean conditions. On either side of the stoichiometric point, a premixed flame branch forms. The excess fuel and oxidizer from the rich and lean branches, respectively, then burn as a downstream diffusion flame branch. For a uniform incoming velocity profile, the premixed branches present a convex surface to the flow, receding downstream owing to the reduction in flame speed with departure from stoichiometry. The three branches motivate the triple flame nomenclature. In a turbulent lifted flame, the incoming velocity profile is likely to be highly nonuniform. Veynante et al. [9] computed triple flames with vortices superimposed on the incoming velocity fields, which distorted the flame branches significantly from the idealized shape; it is also possible that one of the premixed branches may be extinguished while the other continues to burn. Because of these departures from the idealized triple flame structure, the term *leading-edge flame* or *edge flame* is preferred for the description of flame stabilization by partially premixed combustion.

Watson et al. [10] sought to identify edge flame structures in lifted flames explicitly, using CH fluorescence to infer the reaction zone location. The distortion of the edge flame structure noted by Veynante et al., however, makes direct identification difficult in turbulent flames. Another approach [11–14] is to assess edge flame theories by comparing measured flame inflow velocities with both theoretical predictions, and the results of edge flame simulations. Ruetsch et al. [15] performed a theoretical and computational study of triple flames, including heat release effects. For small cross-stream gradients in mixture fraction, the flame propagation speed is [15]

$$U_F \approx S_L(\rho_u/\rho_d)^{1/2}, \tag{1}$$

where U_F is the flame speed relative to the flow well upstream, S_L is the stoichiometric laminar flame

speed, and ρ_u and ρ_d are the densities far upstream and far downstream of the flame. For an upstream stoichiometric methane–air mixture at 298 K, where the downstream mixture consists of combustion products at 2210 K [16], $U_F \approx 2.7 S_L$. When mixture fraction gradients are higher, U_F decreases. This result for U_F is interesting in being significantly smaller than both typical turbulent premixed burning velocities [17], and average axial flow velocities measured at the fixed, mean flame base location, as measured by Schefer et al. [18] using laser-Doppler velocimetry (LDV). Muñiz and Mungal [11], Schefer and Goix [12], Maurey et al. [13], and Han and Mungal [14] measured average axial velocities conditional on flame location, applying PIV in conjunction with measurement of the instantaneous flame base location, and found that the flame tended to stabilize in low-velocity regions of the flow. Flame inflow axial velocities measured by Muñiz and Mungal and by Han and Mungal were typically less than $\approx 3 S_L$. Low inflow velocities are consistent with the edge flame model. It remains to be determined whether the inflow fuel–air mixtures, together with the topology of the reaction rate fields, also agree with the edge flame model.

The goal of this work is to obtain a comprehensive picture of lifted flame inflow conditions by measuring simultaneously the velocity and fuel–air mixing fields immediately upstream of the instantaneous flame location. The measurements have spatial resolution adequate to measure velocity and scalar field gradients. This study will address various outstanding issues, including the relationship between the inflow velocity and scalar fields, the significance of scalar dissipation and the quenching mechanism at the flame base, and the role of the underlying jet flow field in stabilizing the flame. The mixing is quantified by PLIF of acetone seeded into the fuel stream, while the velocity field measurement uses PIV, with glycerol–water fog particles seeded into the co-flowing air as the Mie scattering medium. The high-temperature regions at the flame base are marked by fog evaporation and a drop in the Mie scattering signal [11,19]. Fig. 1 shows the outline of the high-temperature region in a two-dimensional section through the flow centerline. We will use the *leading points*, defined as the most upstream points on the high-temperature interface on either side of the centerline, to infer the flame stabilization location. In this work we will also use the fuel–air mixing information to investigate how the true flame stabilization point, i.e., the most upstream point of the reaction zone, may relate to these leading points.

Table 1
Flow conditions for the lifted jet experiments

Set	u_0	Re_0	θ
I	$10.8\ \mathrm{m\,s^{-1}}$	4400	$12.7d$
II	$15.3\ \mathrm{m\,s^{-1}}$	6200	$18.2d$
III	$18.3\ \mathrm{m\,s^{-1}}$	7400	$21.9d$
IV	$26.4\ \mathrm{m\,s^{-1}}$	10700	$31.7d$

Note. The jet exit bulk velocity is u_0. The jet exit Reynolds number is $\mathrm{Re}_0 \equiv u_e d/\nu$, where u_e is the jet exit excess velocity, $u_e \equiv u_0 - u_\infty$, the jet exit diameter is $d = 4.6$ mm, and the kinematic viscosity of the 85:15 methane/acetone mixture is $\nu = 0.113\ \mathrm{cm^2\,s^{-1}}$. The jet momentum radius is $\theta \equiv [J/(\pi \rho_\infty u_\infty^2)]^{1/2}$, where $J \equiv (\pi d^2/4)\rho_0 u_e^2$ is the jet excess momentum flux.

2. Experimental considerations

These experiments are performed in a vertical, updraft wind tunnel with a 30-cm-square cross section. A 4:1 area ratio contraction inlet, fitted with fine-mesh screens and a honeycomb section, ensures a uniform tunnel flow. The fuel issues from a straight pipe, with outer diameter 6.35 mm, inner diameter 4.6 mm, and length 1.3 m, located on the tunnel centerline. The jet flow is surrounded by an air co-flow with speed $u_\infty = 0.36\ \mathrm{m\,s^{-1}}$. The fuel in these experiments is methane. For diagnostic purposes (Section 2.1), acetone vapor is seeded into the fuel stream to yield an 85:15 methane/acetone mixture (by volume). This mixture has molecular weight 22.35, density $\rho_0 = 0.918\ \mathrm{kg\,m^{-3}}$, and dynamic viscosity $\mu = 1.04 \times 10^{-5}\ \mathrm{N\,s\,m^{-2}}$. The flow conditions for these experiments are given in Table 1.

The large-scale properties of the co-flowing jet, for example the flow width and the mean centerline values of velocity and scalar concentration, observe different scaling regimes, depending on downstream position. In the near field, the flow is expected to scale like a pure jet in a quiescent medium, while in the far field, the flow should follow wake scaling. The appropriate parameter for determining the relevant flow regime is the momentum radius, θ, defined as $\theta \equiv [J/\pi \rho_\infty u_\infty^2]^{1/2}$, where J is the jet excess momentum flux, $J = \rho_0(\pi d^2/4)u_e^2$, and $u_e \equiv u_0 - u_\infty$ is the jet excess velocity. The imaging regions in these measurements extend no further than 1.43θ downstream of the jet exit (Section 2.1), which should be well within the pure jet scaling region of this flow [20].

2.1. Laser imaging methods

Simultaneous PIV and PLIF measure the velocity and scalar concentration fields in the region upstream of the lifted flame. To provide the Mie scattering medium for the PIV, the tunnel flow is seeded

with glycerol/water fog droplets using a commercial fog machine (Rosco 1500). Seeding the tunnel air alone is sufficient to determine the flow velocities in the region just upstream of the flame, because ample coflow air is entrained into the jet as it moves downstream. The fog evaporates at temperatures as low as 100 °C [11], so regions with no Mie scattering signal are interpreted as having been heated by the flame (Section 2.2). A dual-cavity Nd:YAG laser (Spectra-Physics PIV-400), capable of ≈350 mJ/pulse at 532 nm, provides pulse pairs with a temporal spacing of 30 μs, and with a minimum sheet thickness in the measurement area of ≈300 μm. The scattering signal is collected by an interline transfer CCD camera (Kodak Megaplus ES 1.0, 1016 × 1008 pixel resolution), fitted with a Nikon 60-mm $f/2.8$ macro lens, typically stopped down to $f/11$. Each laser pulse is captured in a separate image, allowing the use of a cross-correlation PIV algorithm, which uses iterative interrogation window offset and distortion for enhanced accuracy and vector yield. The final velocity vector results are determined from 16 × 16 pixel subwindows with 50% window overlap.

For the PLIF, acetone vapor is seeded into the methane fuel stream, to approximately 15% by volume. A XeCl excimer laser at 308 nm (Lambda-Physik EMG 203MSC) excites the fluorescence signal. The 308-nm sheet has a minimum thickness of ≈500 μm, and the centers of the 308- and 532-nm sheets are separated by no more than 50 μm, in the sheet-normal direction, throughout the measurement area. The PLIF signal is captured by a thermoelectrically cooled, interline transfer CCD camera (Princeton Instruments Micromax, 515 × 650 pixel resolution), fitted with a Pentax 50-mm lens set at its full $f/1.2$ aperture. With 12-bit signal digitization, the signal-to-noise ratio based on maximum signal level is roughly 100. A bandpass filter (BG 25, 3 mm thickness) isolates the fluorescence signal, which peaks in the range 400–500 nm, from ambient light and flame luminosity. The collection time of the imaging array is set to 1 μs, so the PLIF laser pulse can be placed between the two PIV pulses without the Mie scattering being captured by the PLIF collection camera. Post-processing of the PLIF data corrects for background illumination, nonuniformity in laser sheet intensity, and local laser intensity attenuation caused by passage of the sheet through the fluorescent medium.

The use of acetone PLIF as a concentration diagnostic in combustion experiments is feasible with some caveats. Acetone decomposes at approximately 1000 K [21], and its fluorescence yield varies with temperature. For constant pressure and constant 308-nm laser excitation energy, the fluorescence per unit acetone mole fraction at 330 K is 0.938 (normalized by the value at 296 K), dropping to 0.875 at 374 K, and 0.806 at 424 K [21]. The glycerol–water fog droplets evaporate at as low as 100 °C, so the acetone fluorescence yield is well within 20% of the 296 K value in those areas where Mie scattering from the fog is simultaneously observed, and we can ensure smaller deviations from the 296 K value simply by maintaining a reasonable distance from the high-temperature interface. Finally, differential diffusion effects may arise in using acetone to mark the methane fuel. The acetone–air and methane–air diffusivities are 0.10 and 0.22 cm^2/s, respectively [22]. In combustion, differential diffusion is thought to become significant because of the widely varying diffusivities of different combustion radicals, and because of local laminarization by heat release [23]. As we are concerned primarily with the nonburning region of the lifted flame, and because the relevant diffusivities differ by only a factor of two, we assume that the effect of differential diffusion can be neglected here.

The PLIF measurements directly yield information on the local jet fluid mole fraction, X. From these measurements, we can also determine the jet mixture fraction, Z, defined as the local mass fraction of fluid that originated in the jet. The jet mixture fraction and fuel mole fraction relate as

$$Z = \frac{X M_{\mathrm{f}}}{X M_{\mathrm{f}} + (1 - X) M_{\mathrm{air}}}, \tag{2}$$

where M_{f} and M_{air} are the respective molecular masses of the fuel mixture and air. The mixture fraction, which is a conserved scalar, is commonly used in diffusion flame simulations to represent the molecular mixing, and plays a central role in descriptions of diffusion flame extinction (Section 3.1).

2.2. Flow mapping and high-temperature zone identification

We are also interested here in the gradients of the scalar fields. Achieving the high spatial resolution required for determining gradients accurately is particularly challenging for the scalar field measurements, because it is necessary to include the jet potential core in the images as an absolute reference for determining the jet fluid concentration. The PLIF images must then extend from the jet exit to the location of the flame base, limiting spatial resolution for higher flame lift-off heights. In contrast, the velocity magnitudes in PIV can be determined from the known image dimensions and laser pulse temporal spacing, so the PIV windows can be sized to include only the area around the flame base. Limits on the velocity field resolution will instead come primarily from the resolution capabilities of the PIV algorithm.

Table 2 gives the imaging window geometric parameters. The PLIF window spans from the jet exit,

Table 2
Imaging parameters for the experiments

Set	N	x_s	x_s/θ	(r_{s1}, r_{s2})	(r_{v1}, r_{v2})	(x_{v1}, x_{v2})
I	88	$18.1d$	1.43	$(7.1d, 7.3d)$	$(4.2d, 4.5d)$	$(6.2d, 15.1d)$
II	103	$18.2d$	1.00	$(7.2d, 7.2d)$	$(3.6d, 4.1d)$	$(9.5d, 17.3d)$
III	95	$23.3d$	1.06	$(9.0d, 9.6d)$	$(4.3d, 4.7d)$	$(12.1d, 21.2d)$
IV	90	$26.5d$	0.836	$(10.6d, 10.7d)$	$(4.4d, 5.2d)$	$(14.2d, 23.8d)$

Note. For each set, the number of PLIF/PIV data plane pairs is N. The PLIF imaging window for each case has maximum downstream extent x_s, and spans r_{s1} and r_{s2} on either side of the jet centerline. The PIV imaging windows span from x_{v1} to x_{v2} downstream and r_{v1} and r_{v2} off of the centerline.

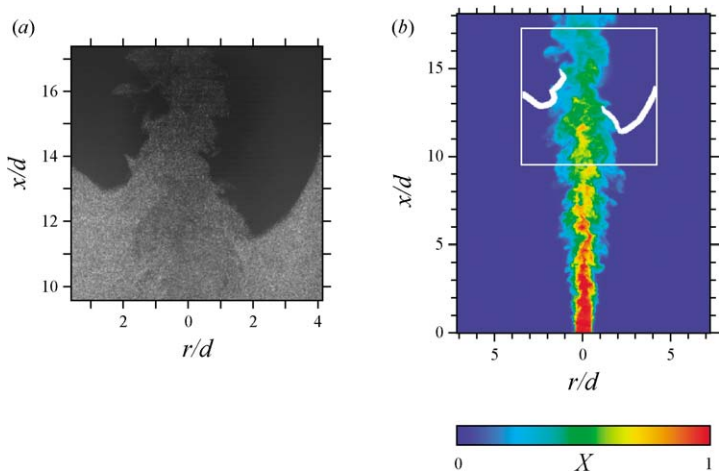

Fig. 2. (a) A sample Mie scattering image, used for PIV, from data set II. (b) The scalar field image, obtained via PLIF, corresponding to the scattering image in (a). The solid window outlines the imaging region for the Mie scattering, and shows the outline of the high-temperature interface determined from (a).

$x = 0$, to an axial location x_s, and straddles the jet axis in the radial direction, extending a distance r_{s1} from the jet centerline to one side, and r_{s2} from the centerline to the other side of the window. The PIV windows span from x_{v1} to x_{v2} downstream, and r_{v1} and r_{v2} to either side of the centerline. Fig. 2a shows a sample Mie scattering image, one of a pair used for PIV, from data set II. Fig. 2b shows the scalar field image, obtained using PLIF, corresponding to the scattering image in (a). The solid window superimposed on the PLIF image is the imaging window used for PIV. The PLIF imaging region extends from the jet nozzle exit to $18.2d$ downstream of the exit, and $7.2d$ to either side of the jet centerline. The Mie scattering image shows a clear distinction between regions of dense light scattering, where temperatures are relatively low and the density of fog particles is high, and regions with no scattering, where the absence of scattering is attributed to fog particle evaporation at elevated combustion temperatures. The interface between the low- and high-temperature regions is determined automatically by filtering the Mie scattering image, and then defining the high-temperature interface as the zone of large brightness gradients. The resulting high-temperature interface for the Mie scattering image of Fig. 2a is superimposed on the corresponding PLIF image in Fig. 2b.

2.3. Leading point positions

No explicit measurement is made here of combustion quantities such as radical concentrations, so we infer the reaction zone location from the high-temperature interfaces [11,19]. The reaction zone is known to be thin (Watson et al. [24] reported CH zones with average thickness ≈1 mm), so we expect the reaction zone to follow these interfaces closely. The leading point, the most upstream point on the measured high-temperature interface on either side of the centerline, will serve as a proxy for the flame stabilization points, which are strictly defined as the most upstream points on the flame zones and are not directly measured. Previous researchers have often assumed that the stabilization points correspond to the leading points. Tacke et al. [25] cast doubt on this assumption, using OH PLIF measurements to infer the instantaneous flame stabilization point, and single-point Raman/Rayleigh/LIPF (laser-induced predisso-

Table 3
Means and standard deviations of the leading point coordinates $(x/d, r/d)$ for the four data sets

Set	Re_0	$\bar{x}/d$	$\sigma_{x/d}$	$\bar{r}/d$	$\sigma_{r/d}$	$\delta(\bar{x})/d$
I	4400	8.62	0.96	1.96	0.28	1.76
II	6200	11.35	0.90	2.25	0.37	2.16
III	7400	14.31	1.26	2.66	0.50	2.58
IV	10700	19.22	1.54	3.31	0.60	3.29

Note. The quantity $\delta(x)$ is an empirical estimate of the jet boundary (Section 3).

ciative fluorescence) to measure temperature, and reporting elevated temperatures upstream of the stabilization points. Watson et al. [24] performed simultaneous CH and OH PLIF measurements at the flame base. The CH radical is short-lived and is thought to mark the instantaneous reaction zone, while OH is removed by slower three-body reactions and marks regions containing hot combustion products. Watson et al. observed that the broad OH zones tend to lie radially outward, and upstream, of the thin CH zones. Using quantitative imaging of OH PLIF gradients, Maurey et al. [13] also observed high-temperature regions outside and upstream of the reaction zones. The leading points can thus not be unambiguously interpreted as the flame stabilization points, though it is safe to assume that the radial and axial motions of the leading points and stabilization points are correlated.

Table 3 gives the means and standard deviations of the leading point coordinates $(x/d, r/d)$ for the four data sets. The table also shows $\delta(\bar{x})$, the radial position of the jet boundary at the mean leading point axial coordinate, where δ is given empirically by Eq. (3) (Section 3). The flame recedes downstream, and the flame position fluctuates more widely, with increasing jet flow rate. Also, it appears that the leading point position tends strongly toward the outer boundary of the jet. The relation of the leading points to the inflow velocity and mixing fields will be explored further in Section 4.

3. Scalar and velocity field evolution

One goal of this work is to relate the stabilization of lifted jet flames to the dynamics and mixing of the underlying turbulent jets. We are interested in whether such quantities as radial profiles of scalar concentration and velocity, or statistics of the scalar and velocity fields, differ when conditioned on proximity of the flame. First we will characterize the scalar and velocity field evolution upstream of the flame. For axisymmetric turbulent jets, it is well established that the scalar and velocity field flow widths scale linearly with downstream distance x, and that the centerline

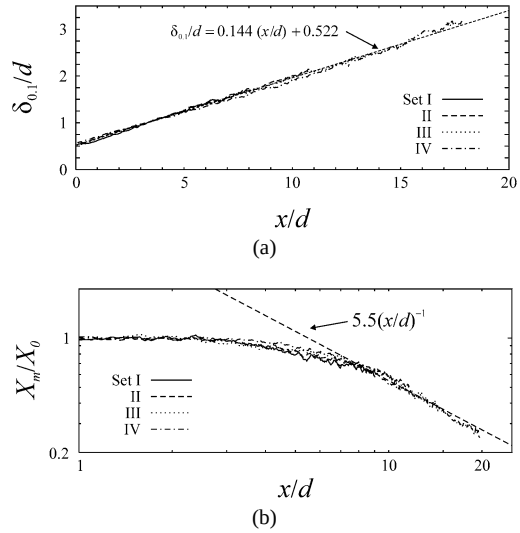

Fig. 3. (a) The scalar field flow width, $\delta_{0.1}$, defined as the half-width of the mean radial scalar profile where the local scalar value is 10% of the centerline value, as a function of downstream coordinate, x, for the four data sets. The dashed line is the least-squares fit to the data. (b) Decay of the centerline mean scalar concentration, X_m, as a function of x for the four data sets. The dashed line is the power law $5.5(x/d)^{-1}$.

mean scalar and velocity values decay as x^{-1}. However, as has been pointed out by George [26], Mi et al. [27], and others, the specific growth and centerline decay rates may depend on the flow initial conditions at the jet nozzle, and may not be universal among different jets. The data compilation of Chen and Rodi [28] also shows considerable scatter in different measurements of growth and decay rates. For this reason, these scalar and velocity field growth and centerline decay rates upstream of the flame must be determined in our particular jet apparatus.

The PLIF measurements allow the characterization of the scalar field evolution throughout the region upstream of the flame. To determine the mean scalar field flow width, the scalar fields for each of the data sets are first conditionally averaged, using only those regions in each image that lie upstream of the lower of the two leading points. The averages thus reflect the nonreacting portion of the jet only. Further, to ensure reasonable statistical convergence, we consider only those spatial locations where the averages include a minimum of 75% of the available data planes. We define the scalar field flow width, $\delta(x)$, as the half-width, at x, of the mean scalar concentration profile between the radial locations at which the concentration is 10% of the centerline value (so $\delta \equiv \delta_{0.1}$). Fig. 3a shows the results for $\delta_{0.1}(x)$ for the four data sets, as determined from the conditionally averaged scalar fields. The growth rates are consistent

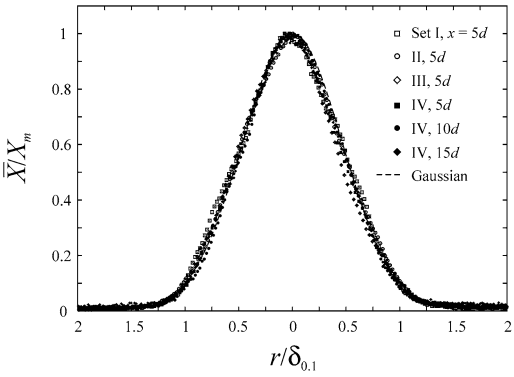

Fig. 4. Radial profiles of normalized mean scalar concentration, $\overline{X}/X_{\mathrm{m}}$, at $x = 5d$ for data sets I, II, and III, and at $x = 5d$, $10d$, and $15d$ for set IV. The radial position is scaled by $\delta_{0.1}$ (Eq. (3)). The dashed line is the Gaussian whose half-width at 10% of maximum is $r/\delta_{0.1} = 1$.

for the four cases, and $\delta_{0.1}$ clearly exhibits a linear dependence on downstream distance. The least-squares linear fit to the data is

$$\delta_{0.1}/d = 0.144(x/d) + 0.522 = 0.144(x/d + 3.63), \quad (3)$$

so the virtual origin for the scalar field evolution is $x/d = -3.63$.

The linearity of $\delta(x)$ results from similarity in the mean radial scalar concentration profiles. Fig. 4 shows the mean radial concentration profiles at $x = 5d$ for data sets I, II, and III, and from data set IV at axial locations $x = 5d$, $10d$ and $15d$. The $\overline{X}$ values are normalized by X_{m}, the centerline values, and the radial positions are normalized by $\delta_{0.1}$. The figure demonstrates that the scalar profiles are self-similar for a given flow and are similar between the different flows, and that the profiles have a Gaussian form.

To determine the decay of the centerline mean scalar concentration, the scalar fields for each of the data sets are again conditionally averaged, but now including the region in each image below the higher of the two leading points. The resulting $X_{\mathrm{m}}(x)$ for the four data sets are shown in Fig. 3b. The end of the potential core, in which $X_{\mathrm{m}}/X_0 = 1$, lies at approximately $x/d = 3$ for each of the curves. By self-similarity and the conservation of the fuel mole fraction in the nonburning region, we expect X_{m} to approach asymptotically an x^{-1} dependence on downstream distance. The figure shows that this dependence is observed beyond approximately $x/d = 8$, and is described well for the four data sets by the function

$$X_{\mathrm{m}} = 5.5(x/d)^{-1}. \quad (4)$$

Fig. 5 shows the PIV results corresponding to the scalar field and Mie scattering image pair represented in Fig. 2. Fig. 5a shows the velocity vector field, subsampled by a factor of 2 in each dimension. Fig. 5b shows a color map of the axial component results for this velocity field. Superimposed on this are two-dimensional streamtraces, determined by fourth-order Runge–Kutta integration on the in-plane PIV velocity component results. While the limited axial extent of the present velocity fields precludes detailed study of the self-similarity of the velocity profiles, we can compare velocity profiles for the different sets in those parts of the PIV windows that are upstream of the typical flame locations. Here, for each data set, we compile the average axial velocity only for those axial locations that are upstream of the lower of the two leading points for 75% of the data planes in that set. Fig. 6 shows radial profiles found from the resulting averaged axial velocity fields. The profiles are of the mean axial excess velocity, $\bar{u} - u_\infty$, and are normalized by the individual profile maxima. The radial positions are scaled by the scalar field half-width, $\delta_{0.1}$ (Eq. (3)). For set I, the profile is for $x = 7d$, for set II, $x = 10d$, for set III, $x = 12.7d$, and for set IV, $x = 15d$. The profiles are in good agreement despite

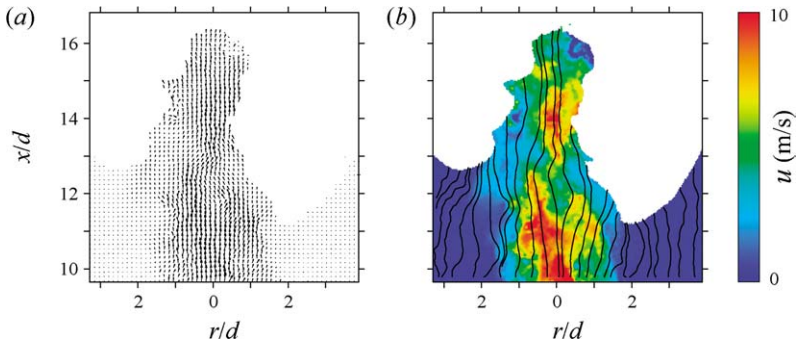

Fig. 5. (a) The PIV velocity vector field determined from the Mie scattering image pair represented in Fig. 2a. (b) The axial component, u, for the PIV results in (a), together with two-dimensional streamtraces determined by a fourth-order Runge–Kutta integration on the in-plane velocity components.

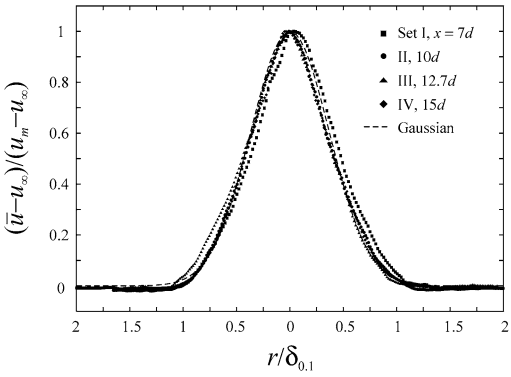

Fig. 6. Radial profiles of normalized mean excess axial velocity, $(\bar{u} - u_\infty)/(u_\mathrm{m} - u_\infty)$, for the four data sets. The dashed line is the Gaussian whose half-width at 10% of maximum is $r/\delta_{0.1} = 0.79$.

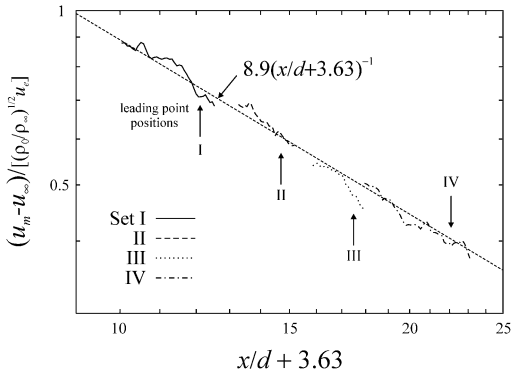

Fig. 7. Decay of the centerline mean excess axial velocity, $u_\mathrm{m}(x)$, for the four data sets. The dashed line is the x^{-1} power law.

the different Reynolds numbers and axial positions. The agreement between the curves using this radial coordinate normalization confirms that the velocity field flow width grows linearly with axial position. A Gaussian curve, with half-width at the 10% points of $r/\delta_{0.1} = 0.79$, is a good fit to these velocity profiles. Thus the ratio of the velocity and scalar field flow widths is 0.79, where Chen and Rodi [28] recommend a value of 0.78. Defining the velocity field flow half-width at the 10% points as $\delta_{\mathrm{u},0.1}$, we can write

$$\delta_{\mathrm{u},0.1}/d = 0.79\delta_{0.1}/d = 0.114(x/d + 3.63). \tag{5}$$

The data also allow the determination of the mean centerline excess axial velocity, u_m, as a function of x. The nonreacting turbulent jet scaling that accounts for the density difference between the jet and ambient fluid, and for different jet exit Reynolds numbers, is $u_\mathrm{m} \propto u_\mathrm{e}(\rho_0/\rho_\infty)^{1/2}(x/d)^{-1}$. Fig. 7 shows the normalized $u_\mathrm{m}(x)$ for the individual data sets. The resulting $u_\mathrm{m}(x)$ curves do not extend from the jet exit, since the velocities are measured only in the subwindows specified in Table 2. The figure shows the expected x^{-1} power law for the nonreacting jet, accounting for the virtual origin, given by

$$\frac{u_\mathrm{m} - u_\infty}{u_\mathrm{e}} = 8.9\left(\frac{\rho_0}{\rho_\infty}\right)^{1/2}(x/d + 3.63)^{-1}. \tag{6}$$

3.1. Scalar dissipation rate field

Important to theories of lifted turbulent jet diffusion flames is the scalar dissipation rate, χ, usually defined using the mixture fraction, Z (Eq. (2)), as

$$\chi \equiv 2D\nabla Z \cdot \nabla Z, \tag{7}$$

where D is the scalar diffusivity. If the flame stabilization mechanism is controlled by local diffusion flame structures, then such structures can be extinguished if the local scalar dissipation rate exceeds a critical threshold determined by the fuel composition. Accurate determination of χ requires that the scalar field measurements have high spatial resolution. To assess the resolution, we will follow the analysis of Su and Clemens [29]. The characteristic length scale of the molecular mixing is defined as λ_D, which can be determined as

$$\lambda_\mathrm{D} = \Lambda\delta\,\mathrm{Re}_\delta^{-3/4}\,\mathrm{Sc}^{-1/2}, \tag{8}$$

where δ is a measure of the flow width, Re_δ is the outer-scale Reynolds number defined using δ, the centerline mean axial excess velocity, $u_\mathrm{m} - u_\infty$, and the kinematic viscosity of air, Sc is the Schmidt number, and Λ is a proportionality constant. When δ is defined as $\delta_{0.05}$, the *full* width at the 5% points of the profile, a variety of studies [30,31] suggest $\Lambda \approx 10$ in axisymmetric jets. This λ_D, which varies with axial location in the jet, is then to be compared to the grid spacing of the scalar field measurements, Δx_X.

A crude resolution requirement is simply for the grid spacing to be smaller than the characteristic scalar mixing length scale, i.e., $\Delta x_\mathrm{X} < \lambda_\mathrm{D}$. More rigorously, one can apply the Nyquist criterion, which requires two grid points per characteristic length scale, or $\Delta x_\mathrm{X} < (\lambda_\mathrm{D}/2)$. Table 4 summarizes the resolution characteristics of the present data sets. To determine λ_D, we apply Eq. (8), using a value of $\Lambda_\mathrm{D} = 10$. For $\delta_{0.05}$, we use the result for the half-width $\delta_{0.1}$ in Eq. (3), and assume a Gaussian profile shape (Fig. 4); for u_m, we use $u_\mathrm{m} = 7(\rho_0/\rho_\infty)^{1/2} \times u_\mathrm{e}(x/d)^{-1}$, which is a reasonable fit to the data in Fig. 7.

The present PLIF results are two dimensional, so only a two-dimensional representation of the scalar dissipation rate, χ_2D, can be measured directly,

Table 4
Resolution parameters for the scalar field measurements

Set	Δx_X (μm)	Re_δ	$x/d : \Delta x_X = \lambda_D(x)$	$x/d : \Delta x_X = \lambda_D(x)/2$	$(\bar{x}/d)_{lp}$	$(\Delta x_X/\lambda_D)_{lp}$
I	129	8000	2.4	8.4	8.62	0.49
II	129	11400	4.2	12.0	11.35	0.52
III	166	13700	7.9	23.1	14.31	0.64
IV	190	20000	14.0	35.2	19.22	0.77

Note. The measurement grid spacing is Δx_X. The outer-scale Reynolds number for each jet is Re_δ. The next two columns give the value of x/d at which the condition $\Delta x_X < \lambda_D$ is first satisfied, and the value of x/d where the Nyquist condition, $\Delta x_X < (\lambda_D/2)$, is satisfied. The mean leading point axial location is $(\bar{x}/d)_{lp}$, and $(\Delta x_X/\lambda_D)_{lp}$ is the relative resolution at the mean leading point axial location.

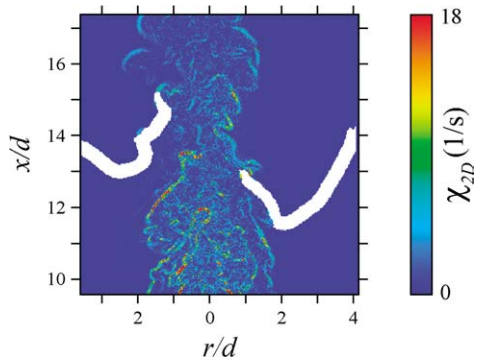

Fig. 8. The measured two-dimensional scalar dissipation rate, χ_{2D}, for the same sample scalar field shown in Fig. 2, shown in the imaging region of the Mie scattering field together with the outline of the high-temperature interface.

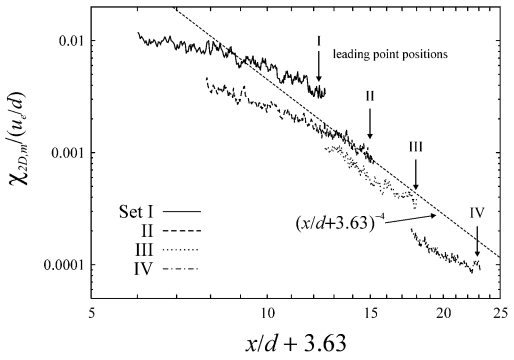

Fig. 9. Axial evolution of the maximum two-dimensional scalar dissipation rate, $\chi_{2D,m}$, normalized by the global strain rate defined by the jet exit excess velocity, u_e, and the jet exit diameter, d. The dashed line is the x^{-4} power law.

namely

$$\chi_{2D} \equiv 2D\left[\left(\frac{\partial Z}{\partial r}\right)^2 + \left(\frac{\partial Z}{\partial x}\right)^2\right] = \cos^2\theta \cdot \chi, \tag{9}$$

where θ is the angle between the true, three-dimensional scalar gradient vector, ∇Z, and the measurement plane. Fig. 8 gives the χ_{2D} result for the scalar field shown in Fig. 2. At these axial positions, Table 4 indicates that the spatial resolution should easily satisfy $\lambda_D < \Delta x$. The χ_{2D} field in Fig. 8 is consistent with prior planar measurements in having a high level of intermittency, with large areas of low dissipation rates, and with high dissipation values concentrated in thin, lamellar structures [29,30] that cover a small volume fraction of the total field. It also appears that high χ_{2D} values are concentrated toward the center of the jet. In particular, at the radial positions of the leading points, and further from the jet centerline, the local χ_{2D} values are much lower than the peaks found within the jet. The relevance of this to stabilization mechanisms is explored in Section 4.3.

Consideration of the axial evolution of χ_{2D} gives a sense of the quantitative accuracy of the χ_{2D} measurements. Unlike the mean scalar and velocity fields, radial profiles of the mean scalar dissipation do not necessarily peak on the jet centerline, so Fig. 9 shows $\chi_{2D,m}$, the maximum values of mean χ_{2D} along radial profiles, for the four data sets. The downstream limit of each curve is the maximum x that is below the downstream leading point in at least 50% of the images in the particular data set, while the upstream limit is the smallest x where the spatial resolution satisfies the criterion $\Delta x_X < \lambda_D(x)$ (Table 4). The dissipation rates are normalized using the global strain rate, u_e/d.

The axial evolution of the maximum mean χ_{2D} should become asymptotically similar, with increasing downstream distance, for the four data sets, in light of the agreement in the axial evolution of the fuel mole fraction and axial velocity component beyond $x/d \approx 8$ (Figs. 3b and 7). (It is not clear that the set I and II curves in Fig. 9 should be similar, because their overlap range is predominantly upstream of $x/d = 8$.) We are mainly interested here in the quantitative accuracy of the measured χ_{2D} near the high-temperature interfaces. The set II curve shows a bend at $x/d + 3.63 \approx 13$, downstream of which χ_{2D} seems to follow the $(x - x_0)^{-4}$ power law expected from classical arguments [32]. The mean leading point position for set II (also shown in the fig-

ure) falls within this scaling range. The set III curve appears to approach the $(x - x_0)^{-4}$ power law fit to the set II data, underestimating the power law by a factor of ≈1.1 at its mean leading point position, $x/d + 3.63 \approx 18$. Set IV also shows evidence of approaching the set II power law dependence, though it underestimates the power law by a factor of ≈ 1.5 at its mean leading point position, $x/d + 3.63 \approx 23$. The quantitative differences in the curves can be explained by the relative resolution of each set (Table 4). At its mean leading point position, set II is just outside Nyquist resolution ($\Delta x_X/\lambda_D = 0.52$), so it is not surprising that the set II curve reflects the expected asymptotic decay of $\chi_{2D,m}(x)$ near the mean leading point position. For sets III and IV, $\Delta x_X/\lambda_D$ at the mean leading point has values 0.64 and 0.77, respectively. Both sets fall short of Nyquist resolution, more noticeably for set IV, which explains its higher degree of underestimation of χ_{2D}.

4. Flame inflow conditions

These measurements allow analyses of the scalar and velocity fields relative to the instantaneous high-temperature interfaces determined as in Section 2.2. These conditional analyses take the form of radial profiles upstream of the leading points, and statistics compiled in regions upstream of the high-temperature interface. Fig. 10 illustrates the parameters used in the analysis.

4.1. Scalar inflow conditions

Fig. 11 shows conditional mean radial profiles of the fuel mole fraction, X, immediately upstream of the high-temperature regions. In each measurement plane, we begin by identifying the leading point on either side of the centerline (Section 2.3). The profile of X is then compiled along the radial line tangent to the leading point. The curves in Fig. 11 represent the averaged profiles for each of the data sets. The figure shows that the mean fuel fraction at the radial position of the leading point for each set is near or below the lean flammability limit. To the outside of the jet, the mean scalar concentration is below the lean limit. The fuel–air mixture on the outside of the high-temperature regions is thus on average not flammable, so the actual reaction zone must typically lie to the inside of the high-temperature regions. The figure also compares each profile with the Gaussian curve with peak value $X_m = 5.5/(\bar{x}/d)$ (Eq. (4)) and half-width at the 10% point given by $\delta_{0.1}/d = 0.144(\bar{x}/d + 3.63)$ (Eq. (3)), where $\bar{x}$ is the mean leading point axial position for each set (Table 3). The Gaussian curves are representative of the unconditional mean radial

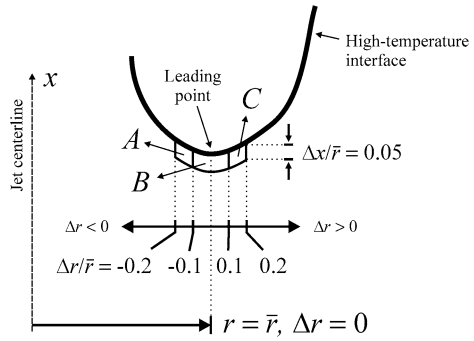

Fig. 10. Schematic of the parameters used in the analysis of instantaneous flame inflow conditions. The coordinate Δr is the radial displacement relative to the leading point position, $\bar{r}$. Compilation of inflow scalar and velocity field statistics uses the three regions A, B, and C that extend $0.05\bar{r}$ upstream from the high-temperature interface.

X profiles (Fig. 4). In each case, the scalar values to the inside of the leading point exceed the values from the unconditional mean profiles. Save for set II, the centerline values for the conditional profiles are also lower than the unconditional peak profile values. The different forms of the conditional and unconditional X profiles suggest a dependence of the leading point position, and by inference, flame stabilization, on local fuel mole fractions near the lean flammability limit, and also with the passage of large-scale mixing structures whose radial profiles are both wider and flatter than the unconditional mean profiles. Further, the disparity in the mean dX/dr values at $\Delta r = 0$, and for $\Delta r < 0$, for the different cases offers evidence that the mean X gradient is not important to the flame stabilization mechanism. (The profiles in Fig. 11 are indistinguishable from profiles compiled at axial positions $5\Delta x_X$ upstream (not shown), indicating that acetone dissociation, and changes in fluorescence efficiency with elevated temperature, are negligible in the locations considered. This suggests that the leading point identification algorithm (Section 2.2) is biased slightly toward the upstream side of the high-temperature interfaces.)

Further information on the true flame location relative to the high-temperature interfaces is provided by considering distributions of the X values along the interfaces. Fig. 12 presents probability densities of X in regions A, B and C as defined in Fig. 10. Fig. 12a shows the X pdfs compiled collectively for sets I–IV. It is clear that in region C, which is radially to the outside of the leading point, the local mixture fraction is predominantly below 0.044, and thus too lean to support combustion. In region B, which is centered radially around the leading point, the pdf is shifted slightly toward higher X values; in region A, inside of the leading point, the pdf differs significantly from

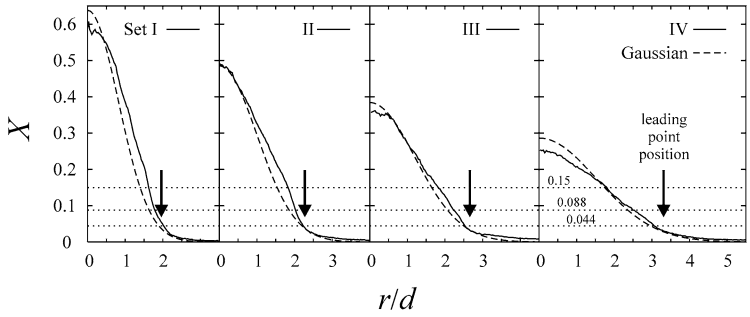

Fig. 11. Conditional mean radial profiles of fuel mole fraction, X, immediately upstream of the instantaneous leading points. Each profile is compared with the Gaussian with half-width at the 10% point and peak value given respectively by Eqs. (3) and (4), evaluated at the mean leading point axial position for each set. The figure also shows the mean leading point radial positions, and the X values corresponding to stoichiometry and the lean and rich flammability limits.

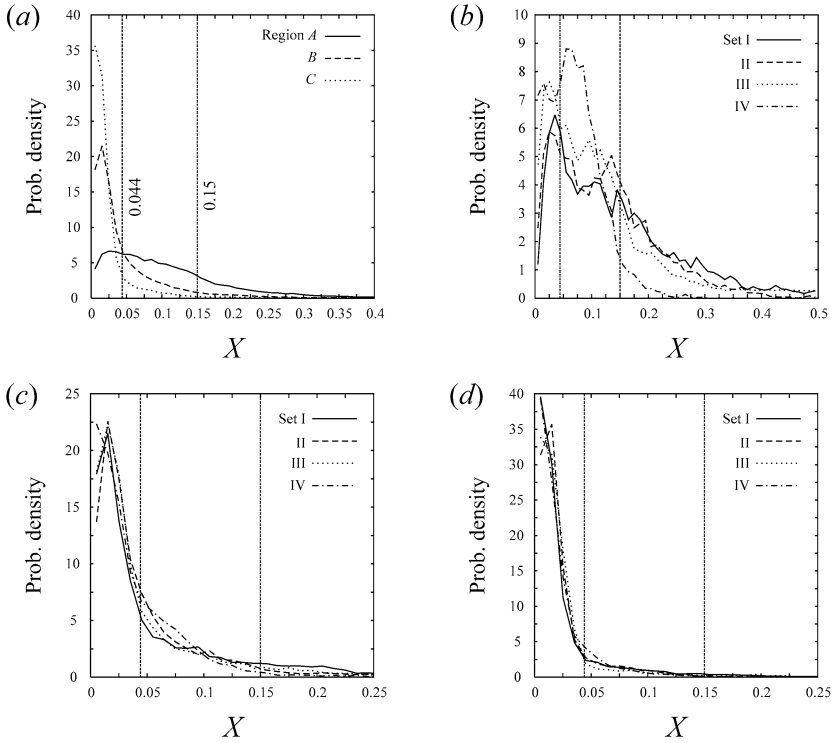

Fig. 12. Probability distributions of scalar concentration, conditional on location on the high-temperature interface. (a) Collective results for sets I–IV: X distributions in regions A, B, and C as defined in Fig. 10. Results for the individual sets: X distributions for (b) region A, (c) region B, and (d) region C.

those for regions B and C, with considerably higher probability densities both between the flammability limits and above the upper limit. Table 5 shows the percentages of X values in the three regions that are below the lower flammability limit, between the lower and upper limits, or above the upper limit. Outside of the leading point, in region C, fully 90% of the X values are below the lower flammability limit, and only 9% are within the limits. In region B, 71% of the X values are below the lower limit, and the probability of being within the limits is up to 24%. In region A, 50% of the X values are within the flammability limits, with the remainder of values fairly symmetrically distributed, with 29% below the lower limit and 21% above the upper limit. The tabulated data confirm the observations from Fig. 12, namely that the actual flame location tends to the lie to the inside of the leading point, because the fuel/air mixture in region A is more likely to be within the flammability limits then in regions B and C.

Table 5
Percentages of X values below, within, and above the flammability limits, in regions A, B, and C, determined from the pdfs in Fig. 12a

Region	$X < 0.044$	$X \in (0.044, 0.15)$	$X > 0.15$
A	29%	50%	21%
B	71%	24%	5%
C	90%	9%	1%

The X pdfs for the individual data sets in the three regions are shown in Figs. 12b–12d. The pdfs in both regions B and C are consistent between the four sets. In region A, there is a noticeable trend toward lower X values as we move from set I to set IV, i.e., as the jet Reynolds number increases and the leading points move further downstream. This trend is consistent with the increased mixing within the jet at higher axial displacements.

4.2. Velocity inflow conditions

Fig. 13 shows conditional mean radial profiles of the axial velocity component, u, immediately upstream of the leading point, for each of the data sets. These profiles are compiled in similar fashion to the fuel mole fraction profiles in Section 4.1. At the mean leading point radial position, the u values for sets I–III are approximately equal to the laminar flame speed, $S_L = 0.43$ m/s, while for set IV, $u \gtrsim S_L$ at that location. There appears to be a minimum in u just to the outside of the leading point, most clearly seen for the set I profile, where the incoming flow decelerates on approaching the high-temperature interface to the outside of the leading point. As r increases further, u approaches u_∞. The figure also shows the Gaussian curve for excess axial velocity for each set whose peak excess velocity value is given by $(u_m - u_\infty) = 8.9 u_e (\rho_0/\rho_\infty)^{1/2} (\bar{x}/d + 3.63)^{-1}$ (Eq. (6)), and where the half-width at the 10% point is the velocity field half-width, $\delta_{u,0.1}$ (Eq. (5)). The Gaussian curves represent the unconditional mean radial $u - u_\infty$ profiles (Fig. 6). The measured profiles can be interpreted similarly to the conditional X profiles of Fig. 11; in particular, the leading point positions correlate with axial velocities near the laminar flame speed, and with instantaneous profiles of axial velocity that are both wider and flatter than the unconditional mean profiles.

Muñiz and Mungal [11] and Han and Mungal [14] previously argued, from PIV measurements, that the highest sustainable stabilization flame speed is $\approx 3S_L$. Comparison of Figs. 11 and 13 for each set shows that the range of r values where the mean X is within the flammability limits correlates well with mean u values between S_L and $3S_L$. Triple flame simulations [15] have similarly observed low incoming fluid velocities. Also seen in triple flame simulations is a drop in the streamwise flow velocity directly upstream of the flame. Fig. 14 shows averaged axial profiles of u upstream of the high-temperature interfaces, both at the leading point radial position ($\Delta r = 0$) and to the inside ($\Delta r/\bar{r} = -0.1$). Moving downstream, the axial velocities first increase, due to the radial spread of the jet, then decrease near the flame (this is particularly evident for sets III and IV), consistent with the triple flame results.

Fig. 15 gives the probability distributions of u/S_L conditional on location on the high-temperature interface. Fig. 15a shows the u/S_L pdfs for regions A–C, compiled collectively for the four sets. As expected, the highest u values are found in region A, nearest the centerline, and the lowest u values are furthest from the centerline, in region C. Figs. 15b–15d give the u/S_L pdfs for the three regions individually for the four data sets. The pdfs are in good agreement despite the different jet Reynolds numbers, which points to a correlation between flame location and local flow velocity. For region A (Fig. 15b), the pdf peaks at $u/S_L = 1$; for regions B and C the peaks in the distribution occur at successively smaller values of u. In region C (Fig. 15d), the most likely u value is less

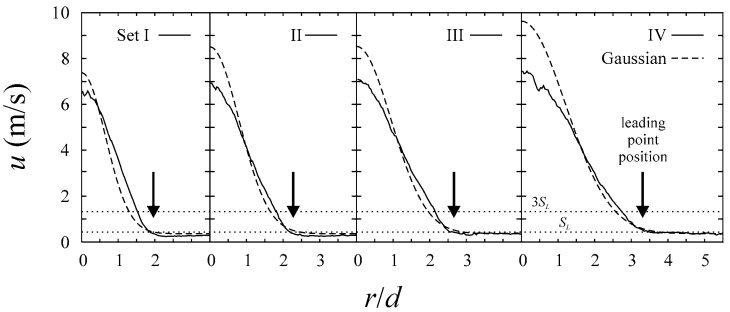

Fig. 13. Conditional mean radial profiles of the axial velocity component, u, immediately upstream of the instantaneous leading points. Each profile is compared with the Gaussian profile of excess axial velocity (Fig. 6) with half-width at the 10% point and peak excess velocity given respectively by Eqs. (5) and (6), evaluated at the mean leading point axial position for each set.

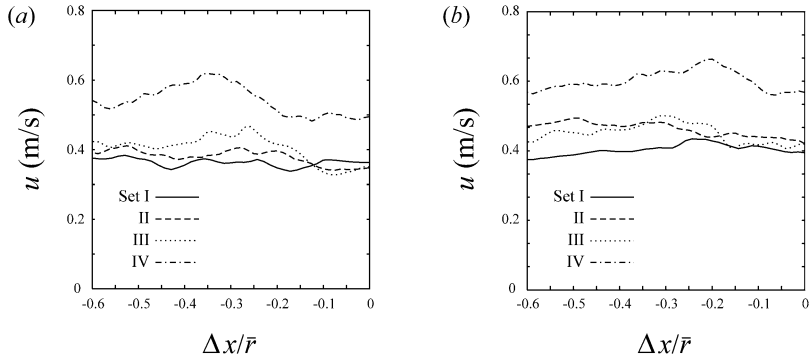

Fig. 14. Averaged axial profiles of the axial velocity, u, fields upstream of the instantaneous high-temperature interface for each of the data sets. (a) The profiles at the leading point radial position, and (b) the profiles for $\Delta r/\bar{r} = -0.1$.

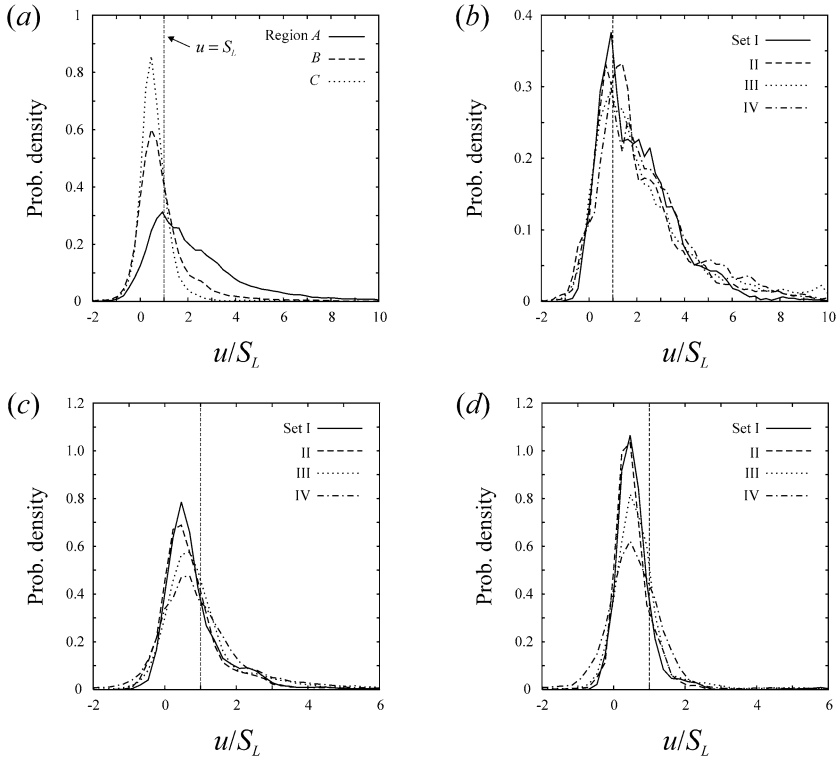

Fig. 15. Probability distributions of the axial component of velocity, conditional on location on the high-temperature interface. (a) Collective results for sets I–IV: u/S_{L} distributions in regions A, B, and C. Results for the individual sets: u/S_{L} distributions for (b) region A, (c) region B, and (d) region C.

than S_{L} and also less than u_{∞}, indicating a deceleration of the incoming flow in that region (see also Figs. 13 and 14).

To explore further the correlation between flow velocity and flame location, Fig. 16a shows probability distributions of axial velocity conditional on local fuel mole fractions within the flammability limits, compiled for sets I–IV in regions A, B, and C. Compared with the unconditional distributions in Fig. 15a, conditioning on flammable mixtures results in increased agreement between the u pdfs in the three regions, which suggests a high correlation between the axial velocity range described by the pdfs and the instantaneous flame location. For X to be within the flammability limits along the high-temperature interface is not a sufficient condition to locate the flame zone, but is a stronger necessary condition than the location of the high-temperature interface alone. The mean axial

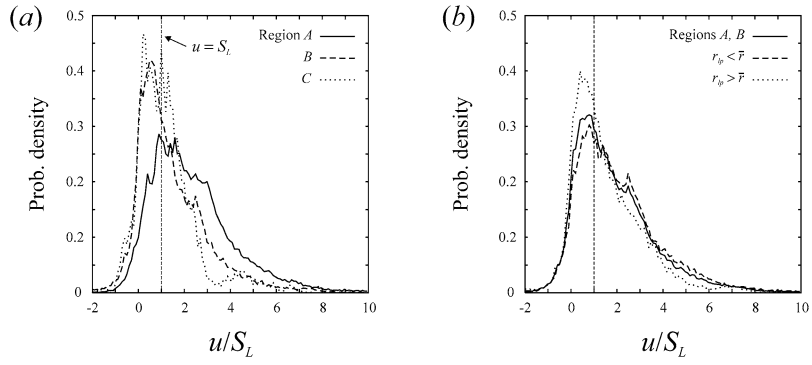

Fig. 16. (a) Probability distributions of the normalized axial component of velocity, u/S_L, in regions A, B, and C, conditional on local jet fuel mole fractions within the flammability limits (compare Fig. 15a). (b) The u/S_L distributions for regions A and B inclusive, conditional on flammable mixtures, for all leading point positions; for leading point radial positions, r_{lp}, inside of the mean position, $\bar{r}$; and for leading point positions outside of the mean position (Section 5).

velocity for the three pdfs in the figure is $u = 1.8S_L$, which is consistent with the low velocities expected from triple flame simulations [15].

4.3. Scalar dissipation rate inflow conditions

In theories for lifted flame stabilization that ascribe a major role to local quenching of thin diffusion flamelets, quenching occurs when the local scalar dissipation rate exceeds a threshold value, which is reported as $\chi_q = 18\ s^{-1}$ for methane–air diffusion flames [33]. If local quenching is indeed important in flame stabilization, then the χ values measured here upstream of the high-temperature interfaces should consistently exceed χ_q. Fig. 17a shows pdfs of the logarithm of the measured, two-dimensional χ_{2D}, compiled over sets I–IV in regions A, B, and C. It is well known that the dissipation rate assumes a nearly log-normal probability distribution [34], which is a Gaussian in semi-log axes, so the figure also shows Gaussian curves having the same first two moments as each of the pdfs. The three pdfs are not in good agreement, with higher χ_{2D} values being found nearer to the jet centerline. The three pdfs do agree reasonably well with their respective Gaussian curve fits.

To correlate local dissipation values more directly with the flame zones, the χ_{2D} pdfs are compiled in regions A–C, conditioned on flammable mixtures, in Fig. 17b. The three conditional pdfs are in good agreement. If quenching were significant, these conditional χ_{2D} pdfs in the near-flame regions would skew toward higher values. Instead, the conditional pdfs maintain the symmetric, nearly Gaussian form of the unconditional pdfs (Fig. 17a). Only 0.06% of χ_{2D} values exceed χ_q. The agreement between the conditional χ_{2D} pdfs probably reflects a correlation between χ_{2D} and the local mixture fraction value. Fig. 17c shows χ_{2D} pdfs conditional on flammable mixtures, both for regions A–C collectively, and for a region with the same radial span as A–C, but which extends from $\Delta x/\bar{r} = 0.4$ to 0.6 upstream of the high-temperature interface. The near-flame pdf is very similar to the upstream pdf, again arguing that flame stabilization is not dependent on the local χ_{2D} values.

The distributions in Figs. 17a–17c represent only the two-dimensional projection of the scalar dissipation rate (Eq. (9)). Prior investigations applied various methods to estimate the three-dimensional χ from two-dimensional scalar measurements. Watson et al. [6] assume that the unmeasured, out-of-plane scalar gradient component is equal to the measured, radial component, giving an estimate of χ as

$$\chi_{est} \equiv 2D\left[2\left(\frac{\partial Z}{\partial r}\right)^2 + \left(\frac{\partial Z}{\partial x}\right)^2\right]. \tag{10}$$

By Eq. (10), $\chi_{est} > \chi_{2D}$ whenever $\partial Z/\partial r \neq 0$. However, this will invariably overestimate χ, not only for instantaneous measurements, but also for probability distributions. For example, if the scalar gradient vector, ∇Z, is distributed isotropically in three-dimensional space, then the highest values of χ should be *equal* to the highest measured two-dimensional χ_{2D}, corresponding to the case where ∇Z lies in the two-dimensional measurement plane.

A more accurate method to find the χ distribution from two-dimensional measurements [34] first recognizes that the measured χ_{2D} distribution is skewed to lower values relative to the χ distribution, because of the projection cosine in Eq. (9). Given the θ distribution, the method reconstructs the χ pdf from the measured χ_{2D} pdf using an inversion procedure. The resulting χ distribution is *exact*, subject to the accuracy of the θ, and measured χ_{2D}, distributions. Fig. 17d shows the χ_{2D} pdf from regions A–C; the same pdf

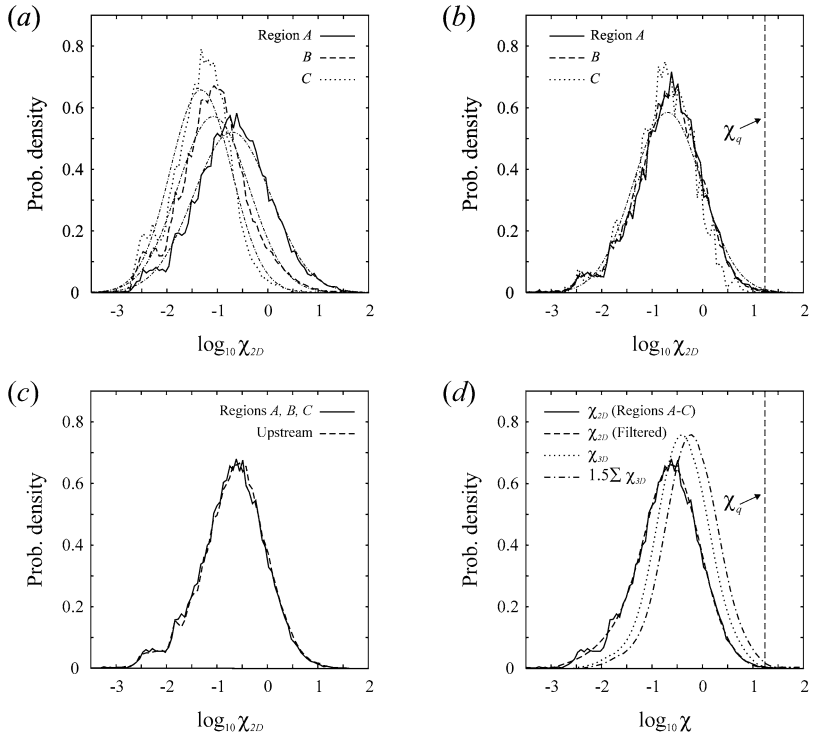

Fig. 17. Probability distributions of the logarithm of the scalar dissipation rate (in units s^{-1}). (a) The measured χ_{2D} distributions in regions A, B, and C, together with their Gaussian fits. (b) The χ_{2D} distributions conditioned on flammable mixtures. The quenching dissipation value is $\chi_q = 18\ s^{-1}$ [33]. (c) The χ_{2D} distribution in regions A–C collectively, and in a window with x between $0.4\bar{r}$ and $0.6\bar{r}$ upstream of the interface. (d) The χ_{2D} distribution compared with estimates of χ_{3D}, computed from the filtered χ_{2D} distribution under the assumption of isotropy [34]. The $1.5 \cdot \chi_{3D}$ pdf represents a worst-case correction for finite spatial resolution (Section 3.1).

after low-pass filtering; and the reconstructed χ_{3D} pdf determined from the filtered χ_{2D} pdf [34], assuming an isotropic distribution of ∇Z. Also indicated in the figure is the quenching scalar dissipation value, $\chi_q = 18\ s^{-1}$. The χ_{3D} pdf is shifted toward higher values relative to the measured χ_{2D}, although the preponderance of χ_{3D} values necessarily remain lower than χ_q. Interpretation of Fig. 17 must bear in mind the resolution limitations mentioned in Section 3.1. It was estimated that the set III and IV data underestimate χ_{2D} by factors of 1.1 and 1.5, respectively, in comparison with the nearly Nyquist-resolved set II. Multiplying all of the dissipation values by the upper bound factor of 1.5 shifts the pdfs in Fig. 17 to the right by 0.18 in the logarithmic scale. Fig. 17d shows the pdf of $1.5 \cdot \chi_{3D}$, where χ_{3D} is the reconstructed three-dimensional dissipation. Even with this resolution correction, only 0.19% of points have $\chi_{3D} > \chi_q$. The location of the high-temperature interfaces is therefore not characterized by upstream dissipation rates exceeding the quenching values, again arguing that local flamelet quenching is not a significant factor in lifted flame stabilization.

5. Dynamics of flame base oscillations

To summarize the foregoing: first, the lifted flame does not alter the scaling and similarity properties of the upstream velocity and mixing fields (Section 3). In particular, the radial velocity and fuel mole fraction profiles are self-similar, with Gaussian form; the profile widths increase linearly with x; and the profile centerline maximum values decay as x^{-1}. Conditional velocity and fuel mole fraction results based on the instantaneous high-temperature interface location (Section 4) show that mean fuel mole fractions at the most upstream point on the interface (the leading point) are near or below the lean flammability limit, indicating that the flame stabilization point is typically radially inside of the leading point. Further, fuel mole fraction profiles immediately upstream of the leading point are typically wider and flatter than the mean similarity profile from the nonreacting part of the jet. In the vicinity of the leading point, and conditional on fuel mole fractions within the flammability limits, the mean axial flow velocity is relatively low, at $1.8S_L$. Finally, conditional scalar dissipation results

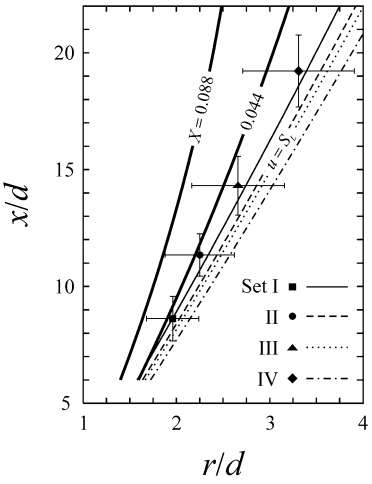

Fig. 18. Relation of the leading point positions to the similarity forms of the mean fuel mole fraction and velocity fields. The similarity forms have Gaussian radial profile shape, with the scalar and velocity field half-widths and profile maxima given by Eqs. (3)–(6). Shown are the mean leading point positions for the four sets, together with intervals representing the standard deviations of the x and r positions; the mean $X = 0.044$ and 0.088 contours, respectively the lean flammability limit and stoichiometric value; and the mean $u = S_L$ contours for the different sets.

(Section 4.3) argue that quenching of laminar diffusion flamelets is not the determining mechanism of turbulent lifted flame stabilization.

From these observations we propose a description of flame stabilization in terms of the interaction of the flame front with the evolution of the nonreacting jet. Fig. 18 shows the mean leading point positions for the four data sets, with intervals representing the standard deviations of the x and r positions. The figure also shows the mean X contours corresponding to the lean flammability limit ($X = 0.044$) and to stoichiometry ($X = 0.088$), as well as the mean $u = S_L$ contours. The $u = S_L$ contours for the four sets differ because of the different jet Reynolds numbers. The contours are determined from the Gaussian similarity forms of the radial profiles of X and u, and from the scaling properties of profile widths and heights given by Eqs. (3)–(6). The mean leading points clearly lie outside of the average lean flammability limit contour. Even allowing that the true flame stabilization point typically lies to the inside of the leading point (Section 2.3; Section 4.1), it is still true that the most upstream point on the flame surface will often lie in a region where the average mixture is nonflammable. In particular, the flame-conditioned X profile is wider and flatter (has a lower peak value) than the mean Gaussian profile (Fig. 11).

This result is explainable in terms of the large-scale organization of jet mixing. Mixing in turbulent jets follows distinct patterns of coherent structures even at high Reynolds numbers [35–38]. Yoda et al. [39] proposed that the jet mixing is organized as a pair of counterrotating helices, which appear as axisymmetric and helical modes in different planar sections through the jet axis. Fig. 19 shows the axisymmetric [35] and helical [37] modes of jet mixing organization. For both modes, individual structures have characteristic length on the order of the jet width. The jet fluid concentration in each structure is made approximately uniform through turbulence, and gradually diminishes through entrainment of ambient fluid as the structure moves downstream. (In Fig. 2b, the relatively large bumps seen on the jet boundary upstream of the high-temperature interfaces offer some evidence of possible large-scale mixing organization in the scalar field.) Fig. 19 also shows sample radial scalar (fuel mole fraction, X) profiles from proximal axial positions for each mode. While all of the profile forms depicted in Fig. 19 contribute to the unconditional mean Gaussian form, it is the widest profiles (represented as the downstream profiles in Fig. 19), which also have the lowest X values on the axis, that dominate the conditional mean. This explains the observed conditional scalar profile shape (Fig. 11).

The flame stabilization process may preferentially seek points further from the centerline because flow velocities are likely to be lower there. Fig. 18 shows that the mean leading points are inside the $u = S_L$ contours, where the average axial velocity slightly exceeds S_L, consistent with the prior observation that the average u is $1.8S_L$ at the leading points. This compares with centerline mean velocities in excess of $15S_L$. We propose a simple model for the dynamics of flame base motion, shown schematically in Fig. 20, based on the large-scale organization of the mixing field, and the tendency of the flame to stabilize in regions of relatively low axial velocity. The figure depicts the axisymmetric mixing mode, but the following discussion is equally valid for the helical mode. Suppose that the stabilization point is initially relatively far from the centerline (Fig. 20a). The axial velocity at this extreme radial location is likely to be lower than the mean flame speed, so that the stabilization point advances upstream. This requires the stabilization point to move radially inward in order to maintain a flammable fuel mole fraction, because the scalar profile is narrower upstream. Moving upstream and toward the centerline also causes the axial flow velocity to increase; eventually, the stabilization point begins to recede downstream (Fig. 20b). A new coherent structure then overtakes the flame. This structure brings a stepwise increase in the fuel mole fraction, and the stabilization point moves radially outward, toward flammable mixtures (Fig. 20c). Together, the downstream and outward motions result in a decreas-

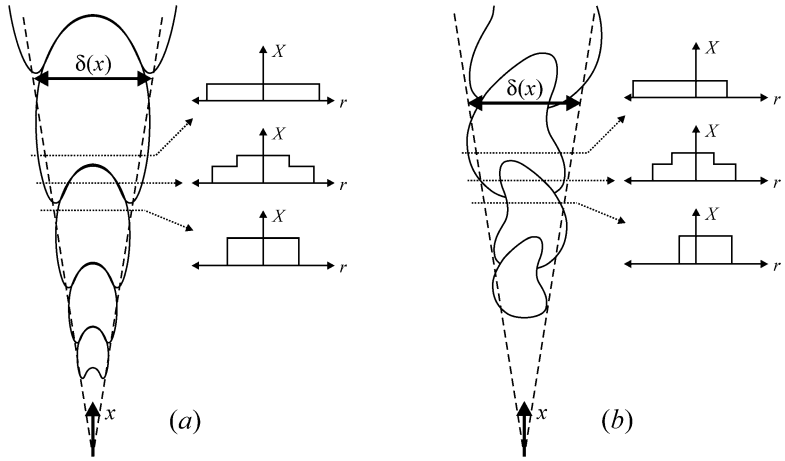

Fig. 19. (a) The axisymmetric mode [35] and (b) the helical mode [37] of jet mixing organization. The individual structures in each mode have approximately uniform jet fluid concentration. Sample radial scalar profiles from each mode of organization are also shown.

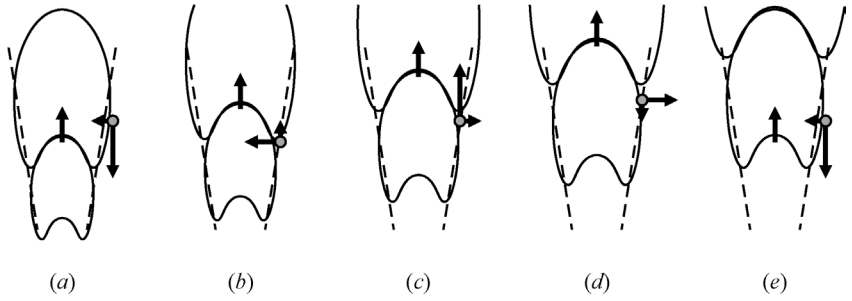

Fig. 20. Schematic depiction of the flame base motion, in terms of the axisymmetric mode of large-scale organization of the mixing field. Time advances from left to right. The instantaneous stabilization point for each time is represented by a gray circle. In (a), the stabilization point is relatively far from the centerline, and the flame advances upstream against the low axial flow velocity. This simultaneously requires that the flame move radially inward, to maintain a flammable mixture. Eventually, the local axial flow velocity becomes sufficiently high that the flame begins to recede downstream (b). When the trailing coherent structure, which brings higher fuel mole fractions, overtakes the flame, the stabilization point moves radially outward (c). As the flame moves downstream and outward, the flow axial velocity decreases, until the flame once again propagates upstream (d) and the initial situation recurs (e).

ing axial flow velocity, eventually causing the stabilization point to advance upstream (Fig. 20d), until the initial situation recurs (Fig. 20e). This description emphasizes the primary role of the large-scale flow organization; small-scale fluctuations and turbulence are higher-order effects.

If this picture of flame base motion is correct, then axial oscillations of the stabilization point will have a period equal to the local passage time of individual large mixing structures. Direct confirmation of this requires simultaneous time-resolved, time series measurements of the scalar field and flame stabilization points, which these data do not provide (the measurement planes are individually time-resolved, but successive planes are more widely separated). However, this description also predicts that higher u values should be found for stabilization points nearer to the centerline, corresponding to a greater likelihood that the flame will propagate downstream, while stabilization points further from the centerline should tend to see smaller u values, corresponding to upstream flame movement. Fig. 16b shows probability distributions of u/S_L, conditional on flammable mixtures, compiled in regions A and B. Separate distributions are compiled for all leading point positions, for leading point positions radially inside of the mean leading point position, and for leading point positions outside of the mean position. Higher axial velocities are found for leading point positions nearer to the centerline. Inside the mean position, the average axial velocity is $u = 2.0S_L$, while outside the mean position, the average u is $1.5S_L$. These results support the above description of flame base motion, where the large-scale flow organization is of primary importance.

These measurements agree with models proposed by Kelman et al. [5] and Upatnieks et al. [40] in ascribing a primary role to partial fuel–air premixing, although differences remain. In the Kelman et al. model, large vortical structures cause local dilution and extinction through air entrainment, forcing the flame to recede downstream; the flame then moves upstream through broad flammable regions generated by upstream mixing, until another vortex is encountered, restarting the cycle. This picture of upstream propagation is at odds with the present observation that the flammable mixtures are consistently to the inside of the measured high-temperature zones. The Upatnieks et al. model ascribes no role to large vortical structures, and instead proposes that the flame modifies the upstream flow to generate a low-velocity, low-turbulence region of flammable mixture into which to propagate. The present measurements suggest, in contrast, that the flame does not actively affect the upstream evolution of either the velocity or scalar field.

6. Conclusions

Planar imaging measurements of fuel mole fractions and radial and axial velocity components, by planar laser-induced fluorescence and particle image velocimetry, respectively, have allowed a thorough investigation of the flow properties in the upstream, stabilization region of turbulent, lifted jet diffusion flames. Four jet Reynolds numbers were considered, ranging from 4400 to 10,700. The diagnostic method delineates the high-temperature region at the base of the lifted flame. The measurements identify the high-temperature interface at the flame base, and show that the flame stabilization point typically lies toward the jet centerline relative to the most upstream point on the interface. Axial velocity values conditional on the flame base position are relatively low, and conditional scalar dissipation rates are below quenching values for laminar diffusion flamelets. These observations are consistent with flame stabilization models based on partial fuel–air premixing. The flame-conditioned scalar and velocity fields are consistent with a description for flame base motions that is based on the large-scale organization of the scalar field. In particular, although the evolution of the jet velocity and scalar fields upstream of the flame is not affected by the combustion, the flame appears preferentially to stabilize toward the outside of the jet, in regions where the local fuel mole fraction axial profiles are wider than the mean profiles, and where incoming flow velocities are relatively low.

Acknowledgments

The authors thank Dr. D. Han and Ms. K.M. Bletzer for assistance with the experiments. This work was supported by the Center for Turbulence Research and the former Gas Research Institute.

References

[1] L. Vanquickenborne, A. van Tiggelen, Combust. Flame 10 (1966) 59–69.
[2] N. Peters, F.A. Williams, AIAA J. 21 (1983) 423–429.
[3] W.M. Pitts, Proc. Combust. Inst. 22 (1988) 809–816.
[4] R.W. Schefer, M. Namazian, J. Kelly, Combust. Flame 99 (1994) 75–86.
[5] J.B. Kelman, A.J. Eltobaji, A.R. Masri, Combust. Sci. Technol. 135 (1998) 117–134.
[6] K.A. Watson, K.M. Lyons, J.M. Donbar, C.D. Carter, Combust. Sci. Technol. 175 (2003) 649–664.
[7] J.W. Dold, Prog. Astronaut. Aeronaut. 113 (1988) 240–248.
[8] J.W. Dold, Combust. Flame 76 (1989) 71–88.
[9] D. Veynante, L. Vervisch, T. Poinsot, A. Liñán, G. Ruetsch, in: Proceedings of the 1994 Summer Program, Center for Turbulence Research, Sanford, CA, 1994, pp. 55–73.
[10] K.A. Watson, K.M. Lyons, J.M. Donbar, C.D. Carter, Combust. Flame 119 (1999) 199–202.
[11] L. Muñiz, M.G. Mungal, Combust. Flame 111 (1997) 16–31.
[12] R.W. Schefer, P.J. Goix, Combust. Flame 112 (1998) 559–574.
[13] C. Maurey, A. Cessou, B. Lecordier, D. Stepowski, Proc. Combust. Inst. 28 (2000) 545–551.
[14] D. Han, M.G. Mungal, Proc. Combust. Inst. 28 (2000) 537–543.
[15] G.R. Ruetsch, L. Vervisch, A. Liñán, Phys. Fluids 7 (1995) 1447–1454.
[16] I. Glassman, Combustion, third ed., Academic Press, San Diego, CA, 1996.
[17] N. Peters, J. Fluid Mech. 384 (1999) 107–132.
[18] R.W. Schefer, M. Namazian, E.E.J. Filtopoulos, J. Kelly, Proc. Combust. Inst. 25 (1994) 1223–1231.
[19] E.F. Hasselbrink, M.G. Mungal, Proc. Combust. Inst. 27 (1998) 867–873.
[20] S. Biringen, An Experimental Study of a Turbulent Axisymmetric Jet Issuing into a Coflowing Airstream, Technical Note 110, von Kármán Institute for Fluid Dynamics, 1975.
[21] M.C. Thurber, F. Grisch, B.J. Kirby, M. Votsmeier, R.K. Hanson, Appl. Opt. 37 (1998) 4963–4978.
[22] R.C. Reid, J.M. Prausnitz, B.E. Poling, The Properties of Gases and Liquids, fourth ed., McGraw–Hill, New York, 1987.
[23] R.W. Bilger, AIAA J. 20 (1982) 962–970.
[24] K.A. Watson, K.M. Lyons, J.M. Donbar, C.D. Carter, Combust. Flame 117 (1999) 257–271.
[25] M.M. Tacke, D. Geyer, E.P. Hassel, J. Janicka, Proc. Combust. Inst. 27 (1998) 1157–1165.

[26] W.K. George, in: W.K. George, R.E.A. Arndt (Eds.), Advances in Turbulence, Hemisphere, 1989, pp. 39–72.
[27] J. Mi, D.S. Nobes, G.J. Nathan, J. Fluid Mech. 432 (2001) 91–125.
[28] C.J. Chen, W. Rodi, Vertical Turbulent Buoyant Jets: A Review of Experimental Data, Pergamon, Oxford, 1980.
[29] L.K. Su, N.T. Clemens, J. Fluid Mech. 488 (2003) 1–29.
[30] K.A. Buch, W.J.A. Dahm, J. Fluid Mech. 364 (1998) 1–29.
[31] M.S. Tsurikov, J.E. Rehm, N.T. Clemens, High-Resolution PIV/PLIF Measurements of a Gas-Phase Turbulent Jet, AIAA Paper 99-0930, 1999.
[32] D.R. Dowling, Phys. Fluids A 3 (1991) 2229–2246.
[33] H.K. Chelliah, K. Seshadri, C.K. Law, in: N. Peters, B. Rogg (Eds.), Reduced Kinetic Mechanisms for Applications in Combustion Systems, Springer-Verlag, Berlin/New York, 1993, pp. 224–240.
[34] W.J.A. Dahm, K.A. Buch, Phys. Fluids A 1 (1989) 1290–1293.
[35] W.J.A. Dahm, P.E. Dimotakis, AIAA J. 25 (1987) 1216–1223.
[36] M.G. Mungal, D.K. Hollingsworth, Phys. Fluids A 1 (1989) 1615–1624.
[37] M.G. Mungal, J.M. O'Neil, Combust. Flame 78 (1989) 377–389.
[38] M.G. Mungal, A. Lozano, I. van Cruyningen, Exp. Fluids 12 (1992) 141–150.
[39] M. Yoda, L. Hesselink, M.G. Mungal, J. Fluid Mech. 279 (1994) 313–350.
[40] A. Upatnieks, J.F. Driscoll, C.C. Rasmussen, S.L. Ceccio, Combust. Flame 138 (2004) 252–272.